SCIENTIFIC REPORTS

OPEN

Dynamic Wavelength-Tunable Photodetector Using Subwavelength Graphene Field-Effect Transistors

François Léonard[1], Catalin D. Spataru[1], Michael Goldflam[2], David W. Peters[2] & Thomas E. Beechem[2]

Dynamic wavelength tunability has long been the holy grail of photodetector technology. Because of its atomic thickness and unique properties, graphene opens up new paradigms to realize this concept, but so far this has been elusive experimentally. Here we employ detailed quantum transport modeling of photocurrent in graphene field-effect transistors (including realistic electromagnetic fields) to show that wavelength tunability is possible by dynamically changing the gate voltage. We reveal the phenomena that govern the behavior of this type of device and show significant departure from the simple expectations based on vertical transitions. We find strong focusing of the electromagnetic fields at the contact edges over the same length scale as the band-bending. Both of these spatially-varying potentials lead to an enhancement of non-vertical optical transitions, which dominate even in the absence of phonon or impurity scattering. We also show that the vanishing density of states near the Dirac point leads to contact blocking and a gate-dependent modulation of the photocurrent. Several of the effects discussed here should be applicable to a broad range of one- and two-dimensional materials and devices.

Photodetectors based on graphene have been extensively studied both experimentally[1–6] and theoretically[7,8]. A number of detector designs harnessing different photocurrent mechanisms have been realized and have shown promising performance. This success brings some interesting questions on whether graphene could provide novel modalities for photodetectors beyond the conventional photoresponse. One such modality is the ability to dynamically tune the spectral sensitivity of the detector. In existing technology, multi-color detection is achieved by using mechanical filters[9], multiple co-located pixels[9], or by using stacked layers[10], all of which have limitations: For example, mechanical filters are slow and introduce unwanted moving parts. In the multi-pixel approach, sub-pixels possessing differing spectral sensitivity are realized by changing material composition during fabrication. While providing hyperspectral response, resolution at a given wavelength is compromised. An alternative design is to stack multiple layers of materials possessing different absorption properties; while this approach is commonly used for two-color detection, generalizing the concept beyond two colors is difficult due to the necessity of monolithically integrating multiple materials and electronically addressing each layer. Furthermore, these methods do not allow for post-fabrication tuning of the spectral band. Thus, a photodetector concept with dynamic tuning of the intrinsic spectral range of a detector pixel composed of a single material possesses advantages over existing technology.

Graphene opens interesting possibilities to realize this concept, as recent work has shown that the *optical* properties of graphene can be modulated using a back gate[11,12] to realize optical modulators. If this result can be translated into modulation of the *photocurrent*, it could be harnessed for tunable photodetector applications. Unfortunately the experimental realization of this concept remains elusive, and to our knowledge the only experimental report of *spectral* photocurrent tunability (by a few tens of nanometers) was realized by inducing conformal changes in graphene[13]. In light of the experimental difficulties and non-idealities implicit in the fabrication of tunable graphene photodetectors, modeling can provide possible paths and identify key roadblocks. Previous

[1]Sandia National Laboratories, Livermore, CA, 94551, United States. [2]Sandia National Laboratories, Albuquerque, NM, 87185, United States. Correspondence and requests for materials should be addressed to F.L. (email: fleonar@sandia.gov)
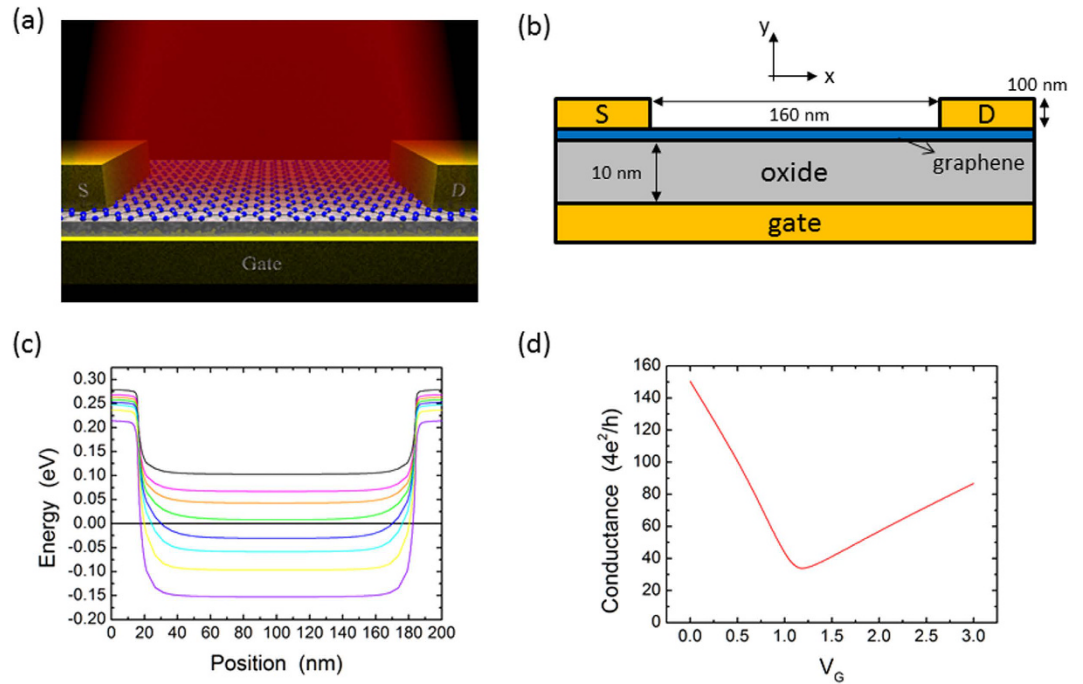
Figure 1. (**a**) Schematic of the photodetector under consideration. A single sheet of graphene is contacted by source and drain electrodes, and is separated from the gate electrode by a dielectric. Monochromatic light illuminates the device. (**b**) Cross-section of the graphene device with the coordinate system and the dimensions used in the simulations. The oxide is lossless and dispersionless with a dielectric constant of 3.9. (**c**) Position of the graphene Dirac point along the length of the FET. Curves from top to bottom correspond to gate voltages of 0, 0.5, 0.75, 1, 1.25, 1.5, 2, and 3 V. (**d**) Dark transfer characteristic at room temperature computed from the band-bending of panel (**c**).

modeling efforts have considered different possibilities for tunable graphene photodetectors based on *multiple* graphene layers, such as bilayer graphene photogating[14] and tunneling between two separate graphene layers[15] or nanoribbons[16]. These exciting results, based on macroscopic transport equations appropriate for long-channel devices, show the promise of devices based on multiple graphene layers. However, since devices based on monolayer graphene are easier to fabricate, an open question is whether wavelength tunability is possible in that case.

In this paper, we address the challenges of identifying promising tunable detector designs and the necessity for more detailed quantum modeling by developing and implementing a non-equilibrium quantum transport approach for photocurrent calculations in graphene devices, including realistic electromagnetic fields. Our main result is that dynamic hyperspectral imaging should be possible in such devices, but a wealth of phenomena renders the system rather complex. For example, we find that translational symmetry breaking due to spatially-varying band-bending and electromagnetic fields leads to a dominance of non-vertical transitions that significantly change the behavior expected from pure vertical transitions and Fermi blocking[17]. We also show that the vanishing density of states at the graphene Dirac point leads to a gate-dependent modulation of the photocurrent due to a contact blocking effect.

Methods

We consider a subwavelength graphene field-effect transistor (FET) as illustrated in Fig. 1a,b. We focus on FETs with short channels for several reasons. First, the recombination time in graphene is on the order of picoseconds[18] which, combined with the Fermi velocity, gives a recombination length of about one micron. Therefore, at low light intensity we can focus on single electron-photon scattering events without recombination. Second, the subwavelength channel leads to a non-uniform vector potential that introduces novel optical transition phenomena. Finally, because we consider uniform illumination of the full device, no temperature gradient exists between the two contacts and photothermoelectric effects[19] can be neglected. While we present results for hot electron devices (i.e. purely ballistic transport), our results can be directly converted to the scattering case by multiplying the calculated photoresponse by the ratio l_{mfp}/L where l_{mfp} is the electron scattering mean free path and L is the channel length.

To calculate the photocurrent, we employ the non-equilibrium Green's function (NEGF) approach, where we explicitly include the electron-photon interaction at the quantum level. We previously developed and applied this approach to carbon nanotube p-n junctions[20]; the graphene FET case differs significantly not only because of the material and the device geometry, but also because the FET does not possess a built-in field to generate a photocurrent at zero bias. Furthermore, to our knowledge, the only NEGF photocurrent calculation for graphene presented in the literature[21] (for a model p-n junction) did not include a non-uniform electromagnetic potential as considered in this paper.

Our calculations consist of two preliminary steps and a final step to obtain the photocurrent, as illustrated in more detail in the Supporting Information. The first preliminary step is a self-consistent NEGF calculation of the potential and charge in the *dark* graphene FET using our previously developed approach for carbon nanotubes[20,22,23] appropriately modified for graphene (specific details can be found in the Supporting Information). In the second preliminary step, we solve Maxwell's equations in the geometry of Fig. 1a,b to obtain the vector potential on the graphene sheet. The final step is to combine the vector potential and the NEGFs from the dark simulations to calculate the photoresponse. Because the graphene FET does not possess a net built-in field, no photocurrent is generated for uniform illumination at zero bias. However, a small source-drain bias breaks the symmetry and leads to a net photocurrent; we therefore focus on the photoconductance in the small bias limit, defined as

$$\sigma^{ph} = \frac{\partial I_{ph}}{\partial V_{sd}}\bigg|_{V_{sd}=0}$$

(1)

where I_{ph} is the photocurrent at a source-drain bias V_{sd}. The full expression for σ^{ph} can be found in the Supporting Information.

In our simulations, we model the graphene using a tight-binding Hamiltonian with overlap integral of 2.5 eV and nearest-neighbor bond length of 0.142 nm. The zigzag direction of the graphene is perpendicular to the electron transport direction. The source and drain electrodes are perfect metals vertically separated from the graphene sheet by a distance of 0.3 nm. Charge transfer between the metal and the graphene is naturally captured in our simulations by using a metal workfunction 0.5 eV larger than graphene. The electron-photon interaction is included by modifying the tight-binding Hamiltonian with the usual $\vec{A} \cdot \vec{p}$ term where $\vec{A}$ is the magnetic vector potential of the light field in the device geometry at the graphene location and $\vec{p}$ is the graphene electron momentum. Details of the implementation can be found in the Supporting Information along with the graphene optical absorption calculated with this NEGF approach.

Results

Figure 1c shows the calculated self-consistent band-bending potential for different gate voltages ranging from 0 V to 3 V (the band-bending potential is equivalent to the energy of the Dirac point). As expected for a FET, the potential in the middle of the channel is modulated by the gate; however, the metal contacts tend to pin the potential, leading to a band-bending over a distance of ~10 nm near the contacts. This length scale is determined by the screening environment of the device and the graphene. In this case, the bottom metal gate provides most of the screening, and the band-bending length scale is determined by the thickness and dielectric properties of the oxide. An additional effect is seen where the band potential under the contacts also changes with the gate bias. This gate modulation of the contacts has been previously discussed in the case of carbon nanotubes[24] and we expect it to be relevant for other one- and two-dimensional materials and devices.

Figure 1d shows the small bias conductance in the dark based on the band-bending potential of Fig. 1c which displays an asymmetric shape and a minimum conductance of about 30 times the quantum of conductance of $4e^2/h$. This result is in good agreement with experimental data for short channel devices[25,26] which come within a factor of three of the minimum conductivity calculated here, and also show prominent asymmetry. In our case, the asymmetry is due to the contact modulation by the gate.

We obtained the vector potential $\vec{A}$ by solving Maxwell's equations in the device geometry of Fig. 1a assuming a periodic structure with perfect metals for the contacts and the bottom gate, for a monochromatic plane wave normally incident and polarized in the x direction (see Supporting Information for details of the calculations). Figure 2a shows that interaction of the plane wave with the device leads to the appearance of an additional component of the vector potential in the y direction. More importantly, the vector potential exhibits strong spatial dependence with significant enhancement near the contacts. Figure 2b shows the ratio of A_x at the contacts to that in the middle of the device, which is about 36 at the longer wavelengths and increases to more than 60 at a wavelength of 1 micron. These results suggest that the properties of photodetectors based on two-dimensional materials should be particularly sensitive to near-contact effects even under flood illumination.

The near-contact focusing of the electromagnetic field is spatially co-located with the device band-bending. As discussed in the context of Fig. 1c, the band-bending near the contact occurs over a distance ~10 nm and is determined by the dielectric thickness. We find that the electromagnetic field also decays over this same length scale as illustrated in Fig. 2c. We believe this is also a consequence of the screening in the device geometry. For example, when solving Maxwell's equations, the boundary conditions at the source and drain electrodes can be satisfied by introducing surface charges and currents, and these will in turn be screened by the bottom gate. We verified this idea by repeating our simulations for different oxide thicknesses, finding that the vector potential decay length (defined as the 1/5 decay distance from the contact) increases with increasing oxide thickness (Fig. 2d).

Having obtained the gate-dependent dark band-bending and the vector potential resulting from illumination, we can calculate the photoconductance. Since the optical absorption in graphene for the out-of-plane contribution is very small[27], we can neglect the A_y component and consider only the spatially-varying A_x component. Figure 3 shows the results of such calculations for two photon energies of 0.1 eV (12.4 μm) and 0.25 eV (4.95 μm). Several conclusions emerge from the data in this figure. First, the photocurrent is gate-tunable for each photon energy. Second, there are regions where clear discrimination between wavelengths is possible. Third, the curves do not follow the simple expectation based on Fermi blocking of vertical transitions. Indeed, if only vertical interband transitions are allowed, the symmetric graphene bands imply that the Fermi level must be less than $\hbar\omega/2$ above or below the Dirac point for transitions to occur. Using the Dirac point energy in the middle of the graphene FET to extract the gate voltage at which transitions should be blocked, we obtain the vertical dashed
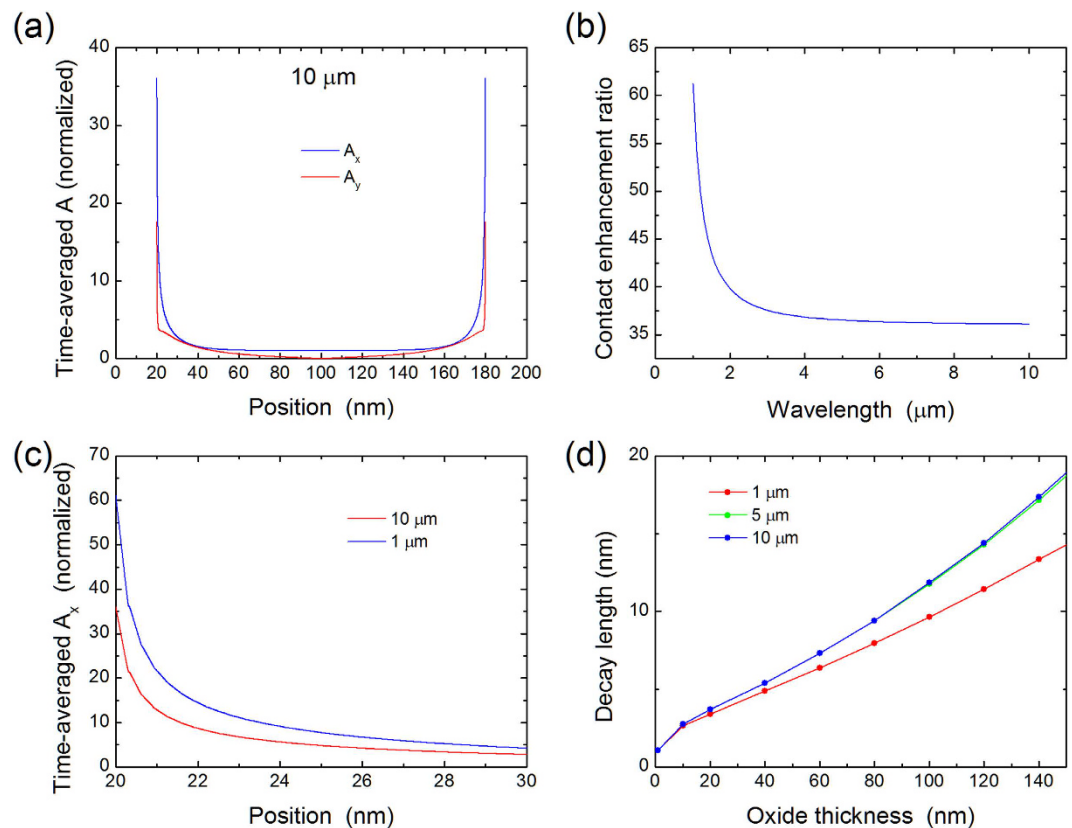
Figure 2. (**a**) Components of the time-averaged vector potential at the graphene sheet for an incoming monochromatic light wave of 10 μm wavelength and polarized in the x direction. The vector potential is normalized to a value of 1 in the middle of the channel. (**b**) Ratio of A_x near the contact to that in the middle of the channel as a function of wavelength. (**c**) Vector potential near the left contact for two different wavelengths of the incoming light. Incoming light polarization is along the x axis. (**d**) Dependence of the decay length of the vector potential as a function of the oxide thickness.
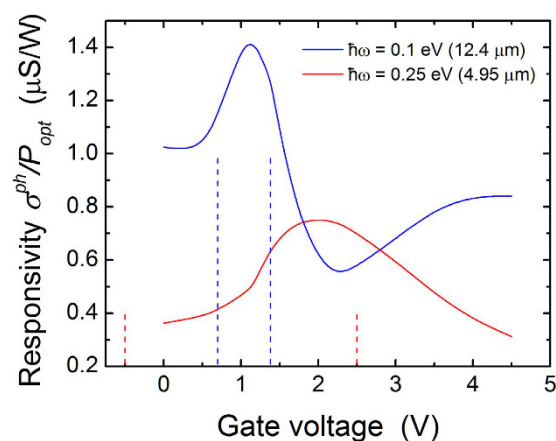
Figure 3. Photoconductance responsivity σ^{ph}/P_{opt} as a function of gate voltage, calculated for two different photon energies. The vertical dashed lines are the boundaries outside of which Fermi blocking would be expected to cut-off the photoresponse.

lines in Fig. 3, outside of which no photocurrent should be observed. The full calculations show a significant deviation from this simple model for both photon energies.

The above effects have their origin in two main factors: non-vertical transitions and gate-dependent contact blocking. Non-vertical transitions can arise when the translational symmetry is broken; in the case of the graphene FET translational symmetry is broken by the spatially-varying electrostatic potential and spatially-varying magnetic vector potential. The missing momentum that allows non-vertical transitions arises
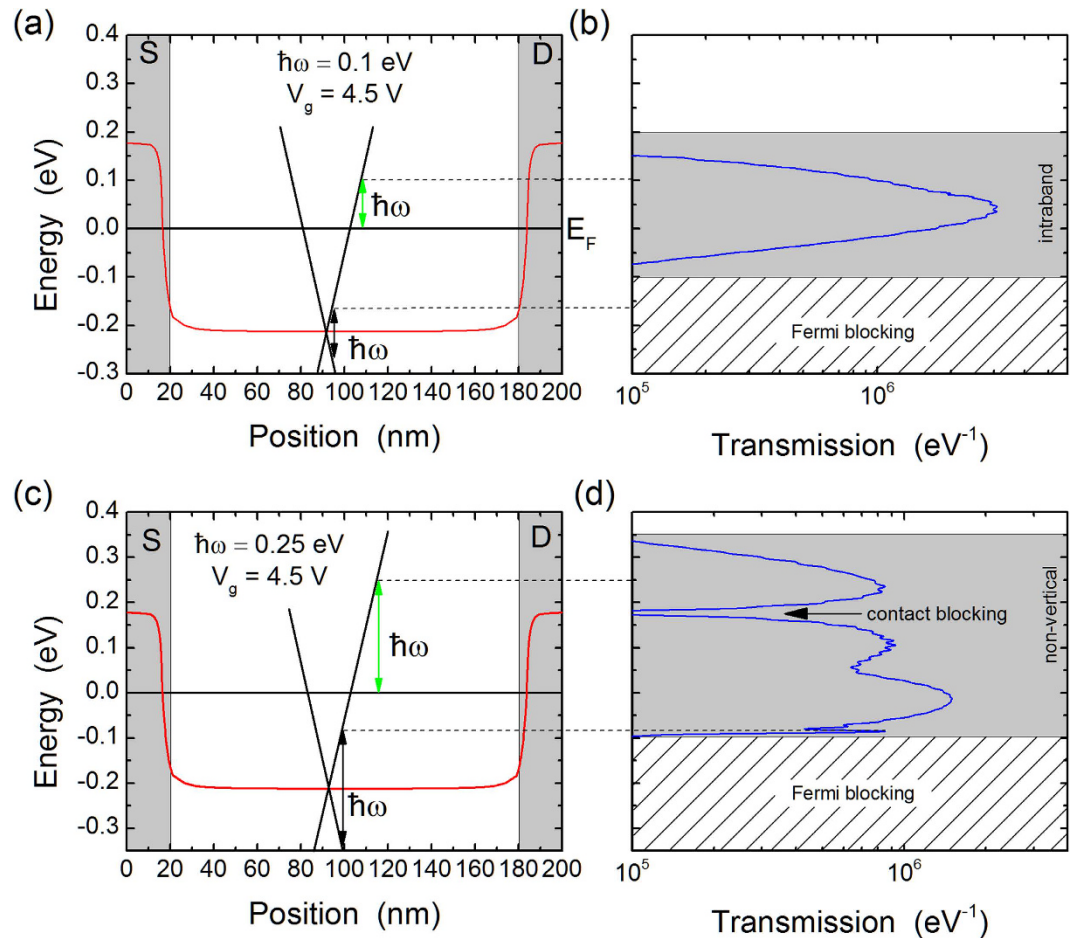
Figure 4. Comparison between the band-bending and the effective transmission probability for photo-excited carriers. The top panels (**a,b**) are for a photon energy of 0.1 eV while the bottom panels (**c,d**) are for a photon energy of 0.25 eV. In both cases the gate voltage is 4.5 V. The vertical grey-shaded regions in the left panels are the source (S) and drain (D) contacts. For illustration purposes, we have also sketched the graphene crossing bands with Dirac point in the middle of the channel. The black vertical arrowed lines denote interband transitions of energy $\hbar\omega$.

from the infinite number of Fourier modes that make up these spatial variations. To illustrate the importance of non-vertical transitions, we plot in Fig. 4 the effective transmission probability for electrons as a function of their energy compared to the band-bending in the graphene FET at a gate voltage of 4.5 V. This transmission represents the probability that an electron injected from the source at energy $E - \hbar\omega$ absorbs a photon and is collected in the drain at energy E. If only vertical transitions were present, the transmission would show a peak at energy $E = \frac{\hbar\omega}{2}$ above the Dirac point. Note that because of the occupancy of the states, at zero temperature the transmission would be non-zero only in an energy window between E_F and $E_F + \hbar\omega$. (Thermal broadening extends this window by a few $K_B T$ above and below.)

For the case of Fig. 4, the Dirac point in the middle of the channel is more than 0.2 eV below the Fermi level. In principle the photoresponse should vanish unless the photon energy is larger than about 0.4 eV. However, we find that for photon energies of 0.1 eV and 0.25 eV, a significant photoresponse remains (Fig. 3). This can be explained from examination of Fig. 4b,d where the interband vertical transitions are Fermi-blocked in both cases but significant transmission is observed at energies where only non-vertical transitions can arise. For example, at $\hbar\omega = 0.1 \, eV$ vertical interband transitions would give a peak at -0.17 eV based on the mid-channel Dirac point, but these transitions are blocked because the Fermi level is at 0 eV and there are no empty states to excite into. However, non-vertical transitions can exist between ≈ -0.1 eV and ≈ 0.2 eV (i.e. the Fermi window plus thermal broadening, and with appropriate momentum transfer from spatial symmetry breaking) in agreement with the transmission. By increasing the photon energy to $\hbar\omega = 0.25 \, eV$ we see the appearance of another effect: contact blocking. Indeed, at this photon energy, non-vertical transitions exist up to energies of 0.25 eV (plus thermal broadening). However, the transmission function has a strong dip to zero in the middle of this range at an energy that corresponds to the Dirac point in the contacts. This strong reduction in transmission is a consequence of the density of states of graphene that goes to zero at the Dirac point; thus, one can think of this effect as contact blocking of the photocurrent.
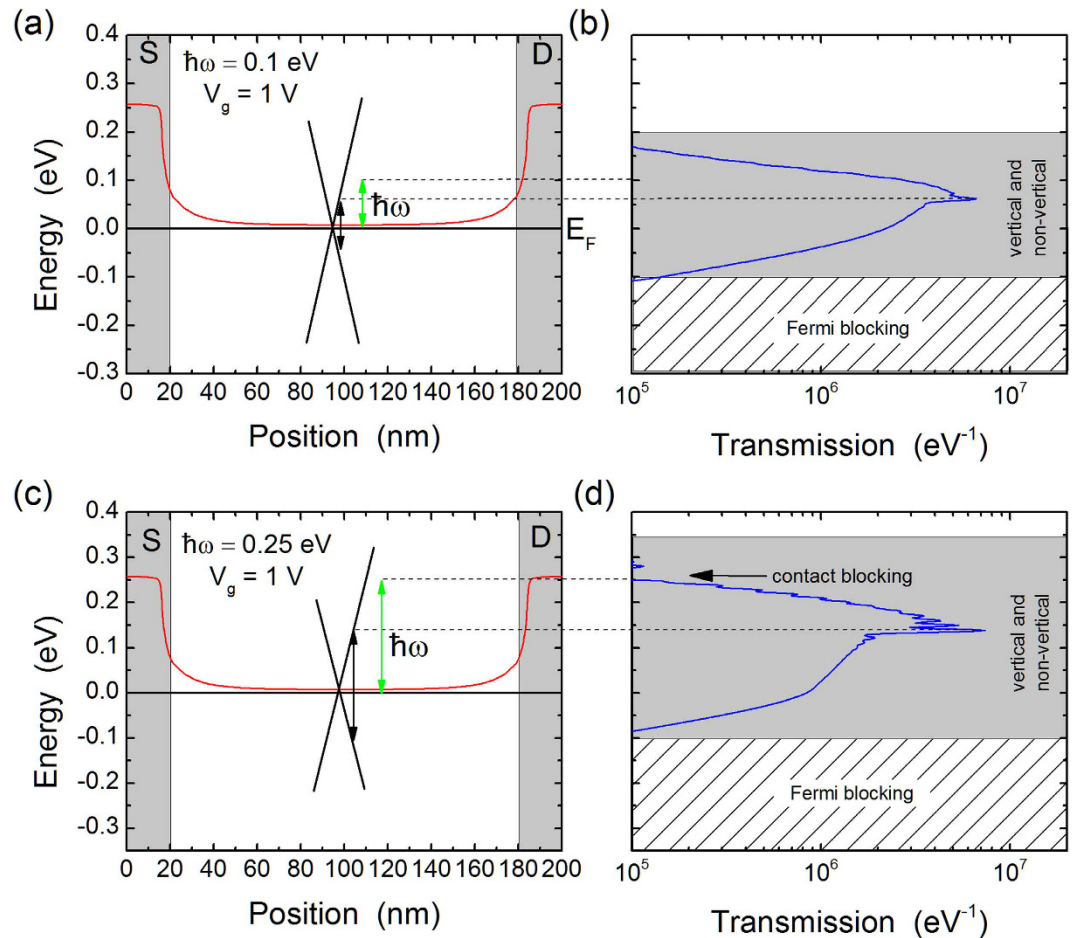
Figure 5. Comparison between the band-bending and the effective transmission probability for photo-excited carriers. The top panels (**a,b**) are for a photon energy of 0.1 eV while the bottom panels (**c,d**) are for a photon energy of 0.25 eV. In both cases the gate voltage is 1 V. The vertical grey-shaded regions in the left panels are the source (S) and drain (D) contacts. For illustration purposes, we have also sketched the graphene crossing bands with Dirac point in the middle of the channel. The black vertical arrowed lines denote vertical interband transitions of energy $\hbar\omega$.

This effect is in part responsible for the shape of the photoresponse versus gate voltage observed in Fig. 3. To illustrate this effect in more detail, Fig. 5 plots the band-bending and transmission probabilities for a gate voltage of 1 V. In the case of $\hbar\omega = 0.1 \ eV$ a small peak at 0.061 eV is visible due to vertical transitions, but most of the photoresponse comes from non-vertical transitions. A similar situation arises for $\hbar\omega = 0.25 \ eV$; however, the Dirac point in the contact regions is now located in the Fermi window and blocks a significant portion of the carriers, leading to a reduced photoresponse and the unusual shape observed in Fig. 3.

To further determine the factors that lead to the unusual importance of non-vertical transitions, we calculated the transmission for a gate voltage of 1 V and illumination at $\hbar\omega = 0.1 \ eV$. For this gate voltage, the Dirac point is 0.011 eV above the Fermi level in the middle of the channel and vertical interband transitions should give a peak at an electron energy of 0.061 eV. As shown in Fig. 6, a peak is observed at this energy, but is significantly broadened by non-vertical transitions. We then repeated this calculation for a constant electrostatic potential throughout the device (i.e. flat bands) with a value corresponding to the Dirac point in the middle of the channel for the full device simulations at $V_g = 1 V$. Figure 6 shows that at low temperatures (30 K in this case) and for a uniform vector potential in the channel, there is a narrow peak due to vertical interband transitions; increasing the temperature to 300 K does not change this behavior and we therefore rule out temperature effects as the main source of the non-vertical transitions. However, introducing a non-uniform vector potential (but still with flat bands) gives a much broader peak, implying that the non-uniform light profile itself leads to significant non-vertical transitions. Finally, since the full device band-bending gives an even broader peak, non-vertical transitions are also enhanced by the spatially-varying band-bending that breaks the spatial symmetry and provides the momentum. (Additional details of how these effects emerge from the NEGF formalism can be found in the Supporting Information.)
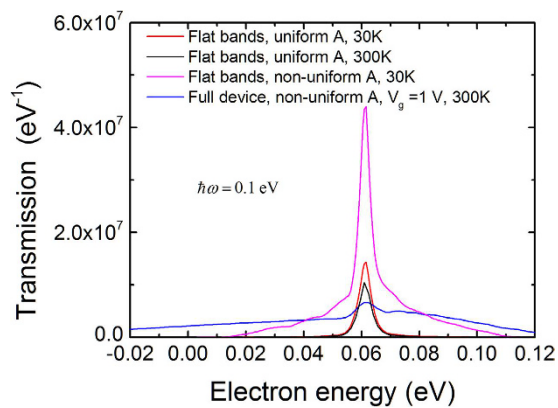
Figure 6. Electron transmission for a photon energy of 0.1 eV and a full device band-bending for a gate voltage of 1 V. The result is compared with different flat band cases.

Conclusion

In conclusion, we find that monolayer graphene FETs open a new avenue to realize photodetectors with dynamic spectral tunability, and display a number of novel underlying phenomena that should be general. For example, electromagnetic field focusing at the contacts plays a key role in governing photoresponse behavior, a phenomenon that should apply to a broad range of one- and two-dimensional materials. We also expect that non-vertical transitions induced by symmetry breaking due to the spatial variations of the band-bending and the vector potential should also become prominent in other low-dimensionality materials. Finally, additional studies are needed to assess the robustness of the wavelength tunability to non-ideal factors such as substrate charged impurities. Nonetheless, our work establishes the first framework to guide and interpret experimental and theoretical efforts.

References

1. Koppens, F. H. L. *et al.* Photodetectors based on graphene, other two-dimensional materials and hybrid systems. *Nat. Nanotechnol.* **9,** 780–793 (2014).
2. Xia, F., Mueller, T., Lin, Y.-m., Valdes-Garcia, A. & Avouris, P. Ultrafast graphene photodetector. *Nat. Nanotechnol.* **4,** 839–843 (2009).
3. Echtermeyer, T. J. *et al.* Strong plasmonic enhancement of photovoltage in graphene. *Nat. Commun.* **2,** 458, doi: 10.1038/ncomms1464 (2011).
4. Liu, Y. *et al.* Plasmon resonance enhanced multicolour photodetection by graphene. *Nat. Commun.* **2,** 579, doi: 10.1038/ncomms1589 (2011).
5. Singh, R. S., Nalla, V., Chen, W., Wee, A. T. S. & Ji, W. Laser patterning of epitaxial graphene for schottky junction photodetectors. *ACS Nano* **5,** 5969–5975 (2011).
6. Gabor, N. M. *et al.* Hot carrier–assisted intrinsic photoresponse in graphene. *Science* **334,** 648–652 (2011).
7. Ryzhii, V., Mitin, V., Ryzhii, M., Ryabova, N. & Otsuji, T. Device model for graphene nanoribbon phototransistor. *Appl. Phys. Express* **1,** 063002 (2008).
8. Ahmadi, E. & Asgari, A. Modeling of the infrared photodetector based on multi layer armchair graphene nanoribbons. *J. Appl. Phys.* **113,** 093106 (2013).
9. Rogalski, A., Antoszewski, J. & Faraone, L. Third-generation infrared photodetector arrays. *J. Appl. Phys.* **105,** 091101 (2009).
10. Rogalski, A. Infrared detectors: An overview. *Infrared Physics & Technology* **43,** 187–210 (2002).
11. Yao, Y. *et al.* Wide wavelength tuning of optical antennas on graphene with nanosecond response time. *Nano Lett.* **14,** 214–219 (2014).
12. Li, Z. Q. *et al.* Dirac charge dynamics in graphene by infrared spectroscopy. *Nat. Phys.* **4,** 532–535 (2008).
13. Kang, P., Wang, M. C., Knapp, P. M. & Nam, S. Crumpled graphene photodetector with enhanced, strain-tunable, and wavelength-selective photoresponsivity. *Adv. Mater.* **28,** 4639–4645 (2016).
14. Ryzhii, V. & Ryzhii, M. Graphene bilayer field-effect phototransistor for terahertz and infrared detection. *Phys. Rev. B* **79,** 245311 (2009).
15. Ryzhii, V. *et al.* Voltage-tunable terahertz and infrared photodetectors based on double-graphene-layer structures. *Appl. Phys. Lett.* **104,** 163505 (2014).
16. Ryzhii, V., Ryzhii, M., Ryabova, N., Mitin, V. & Otsuji, T. Graphene nanoribbon phototransistor: Proposal and analysis. *Jpn. J. Appl. Phys.* **48,** 04C144 (2009).
17. Mak, K. F. *et al.* Measurement of the optical conductivity of graphene. *Phys. Rev. Lett.* **101,** 196405 (2008).
18. George, P. A. *et al.* Ultrafast optical-pump terahertz-probe spectroscopy of the carrier relaxation and recombination dynamics in epitaxial graphene. *Nano Lett.* **8,** 4248–4251 (2008).
19. Tielrooij, K. J. *et al.* Hot-carrier photocurrent effects at graphene–metal interfaces. *J. Phys. Condens. Matter* **27,** 164207 (2015).
20. Stewart, D. A. & Léonard, F. Photocurrents in nanotube junctions. *Phys. Rev. Lett.* **93,** 107401 (2004).
21. Chen, J., Hu, Y. & Guo, H. First-principles analysis of photocurrent in graphene *PN* junctions. *Phys. Rev. B* **85,** 155441 (2012).
22. Léonard, F. & Stewart, D. A. Properties of short channel ballistic carbon nanotube transistors with ohmic contacts. *Nanotechnology* **17,** 4699 (2006).
23. Kienle, D., Vaidyanathan, M. & Léonard, F. Self-consistent ac quantum transport using nonequilibrium green functions. *Phys. Rev. B* **81,** 115455 (2010).
24. Cummings, A. W. & Léonard, F. Enhanced performance of short-channel carbon nanotube field-effect transistors due to gate-modulated electrical contacts. *ACS Nano* **6,** 4494–4499 (2012).
25. Han, S. J., Chen, Z., Bol, A. A. & Sun, Y. Channel-length-dependent transport behaviors of graphene field-effect transistors. *IEEE Electron Device Lett.* **32,** 812–814 (2011).
26. Hollander, M. J. *et al.* Short-channel graphene nanoribbon transistors with enhanced symmetry between p- and n-branches. *Appl. Phys. Express* **7,** 055103 (2014).
27. Marinopoulos, A. G., Reining, L., Rubio, A. & Olevano, V. *Ab initio* study of the optical absorption and wave-vector-dependent dielectric response of graphite. *Phys. Rev. B* **69,** 245419 (2004).

Author Contributions

All authors contributed to development of the project and writing of the manuscript. F.L., C.S., and M.G. performed the computational work.

Additional Information

Supplementary information accompanies this paper at http://www.nature.com/srep

Competing Interests: The authors declare no competing financial interests.

How to cite this article: Léonard, F. *et al.* Dynamic Wavelength-Tunable Photodetector Using Subwavelength Graphene Field-Effect Transistors. *Sci. Rep.* **7**, 45873; doi: 10.1038/srep45873 (2017).

Publisher's note: Springer Nature remains neutral with regard to jurisdictional claims in published maps and institutional affiliations.